OPTICS

Efficient ultrafast all-optical modulation in a nonlinear crystalline gallium phosphide nanodisk at the anapole excitation

Gustavo Grinblat[1]*, Haizhong Zhang[2], Michael P. Nielsen[3], Leonid Krivitsky[2], Rodrigo Berté[4], Yi Li[4,5], Benjamin Tilmann[4], Emiliano Cortés[4], Rupert F. Oulton[6], Arseniy I. Kuznetsov[2], Stefan A. Maier[4,6]

High–refractive index nanostructured dielectrics have the ability to locally enhance electromagnetic fields with low losses while presenting high third-order nonlinearities. In this work, we exploit these characteristics to achieve efficient ultrafast all-optical modulation in a crystalline gallium phosphide (GaP) nanoantenna through the optical Kerr effect (OKE) and two-photon absorption (TPA) in the visible/near-infrared range. We show that an individual GaP nanodisk can yield differential reflectivity modulations of up to ~40%, with characteristic modulation times between 14 and 66 fs, when probed at the anapole excitation (AE). Numerical simulations reveal that the AE represents a unique condition where both the OKE and TPA contribute with the same modulation sign, maximizing the response. These findings highly outperform previous reports on sub–100-fs all-optical switching from resonant nanoscale dielectrics, which have demonstrated modulation depths no larger than 0.5%, placing GaP nanoantennas as a promising choice for ultrafast all-optical modulation at the nanometer scale.

INTRODUCTION

Nonlinear optical effects occur when intense electromagnetic fields interact with matter. Although intrinsically weak, nonlinear optical processes can grow to be very strong if the so-called phase-matching condition is achieved, provided that the nonlinear interaction length is much longer than the participating wavelengths (*1*). At the nanometer scale, however, these conditions cannot be met, as the characteristic distances are of the order of a single wavelength or even smaller. Recently, low-loss nonlinear dielectric nanoantennas and metasurfaces have been explored to enhance nonlinear interactions at subwavelength volumes by exploiting resonant effects (*2*–*25*). Nanoantennas and metasurfaces made using dielectric materials with high refractive index and high nonlinear susceptibility can be designed to spectrally selective and efficiently confine light fields inside the nonlinear dielectric. This approach maximizes both the excitation density and the nonlinear interaction volume while keeping losses at a minimum. Using this strategy, photonic nanoantennas using silicon (*7*, *17*, *23*), germanium (*5*, *6*), gallium phosphide (GaP) (*4*, *25*), and aluminum gallium arsenide (AlGaAs) (*8*, *24*) have been shown to produce second- and third-harmonic generation efficiencies of several orders of magnitude larger than in bulk. Moreover, those reports demonstrate that dielectric nanoresonators can highly outperform their relevant plasmonic counterparts (*26*–*28*).

Nonlinear optical phenomena other than nonlinear frequency conversion have also been investigated in resonant dielectric nanostructures. For example, the nonlinear optical Kerr effect (OKE) and two-photon absorption (TPA) have been studied for ultrafast modulation of optical reflectivity and transmission in silicon-based nanoantennas and metasurfaces (*2*, *3*). The OKE and TPA are third-order nonlinear effects that can instantaneously vary the real and imaginary parts of the complex refractive index of a medium (*1*), respectively, enabling femtosecond control of its optical properties. Modulation depths, defined as [peak differential reflectivity/transmissivity] − [baseline modulation], of up to ~0.5% at sub–100-fs time scales have been demonstrated for the silicon nanosystems at visible and near-infrared wavelengths (*2*, *3*). However, substantially larger modulation depths are required before such nonlinear modulators can become suitable for applications.

Ultrafast all-optical switches are expected to become a core element in high-speed operating integrated photonic applications using photons as information carriers, such as optical computing and communication, and quantum information processing (*29*, *30*). The four main performing indices of an all-optical switch are switching time, switching efficiency, control power, and characteristic size. Ideally, an all-optical switch should feature <100-fs OFF-ON-OFF response times, switching efficiencies close to 100%, <0.1-pJ control light energies, and <1-μm characteristic size. However, no known structure to date behaves as an ideal switch.

One possible candidate to improve on the reported modulation performance is GaP. Compared to silicon, GaP presents negligible linear absorption and has larger Kerr nonlinear index (n_2) and TPA coefficient (β) over the whole of the visible and the blue end of the near-infrared spectrum (*31*–*33*). Furthermore, it has been shown that bulk crystalline GaP can produce modulation depths as high as 70% (*32*). Nanostructuring the surface of bulk GaP to form nanoantennas has also been used to enhance nonlinear second harmonic generation and multiphoton absorption photoluminescence (*4*, *25*). However, the absence of index contrast between such GaP nanoresonators and a substrate naturally limits the field confinement that can be attained. Here, we study the nonlinear dynamics of individual

[1]Departamento de Física, FCEN, IFIBA-CONICET, Universidad de Buenos Aires, C1428EGA Buenos Aires, Argentina. [2]Institute of Materials Research and Engineering, A*STAR (Agency for Science, Technology and Research), 138634, Singapore. [3]School of Photovoltaic and Renewable Energy Engineering, University of New South Wales, Sydney, NSW 2052, Australia. [4]Chair in Hybrid Nanosystems, Nanoinstitut München, Fakultät für Physik, Ludwig-Maximilians-Universität München, 80539 München, Germany. [5]School of Microelectronics, MOE Engineering Research Center of Integrated Circuits for Next Generation Communications, Southern University of Science and Technology, Shenzhen, 518055 Guangdong, China. [6]The Blackett Laboratory, Department of Physics, Imperial College London, London SW7 2AZ, UK.
*Corresponding author. Email: grinblat@df.uba.ar

crystalline GaP nanodisks on silicon dioxide (SiO_2) through nondegenerate pump-probe spectroscopy in the 600- to 1000-nm wavelength region using sub–10-fs pulses. We demonstrate that a single resonant GaP nanodisk of 0.05-μm^3 volume can reach modulation depths near 40%, with a temporal full width at half maximum (FWHM) of 66 fs. Nonlinear numerical simulations considering the OKE and TPA show excellent agreement with the experimental measurements and unveil the individual contributions of the different nonlinear phenomena to the overall response.

RESULTS AND DISCUSSION

Nanodisks made of metal-organic chemical vapor deposition (MOCVD)–grown crystalline GaP were patterned on a SiO_2 (10 μm)/sapphire (150 μm) substrate through electron-beam lithography (EBL) (refer to Materials and Methods for fabrication details). The GaP nanodisks were of 200 nm in height and 500 to 700 nm in diameter (D), with a center-to-center pitch of 3 μm to prevent optical coupling between adjacent structures (see a representative scanning electron microscopy image of the sample in Fig. 1A). To identify the resonances of the fabricated nanoantennas, we simulated their scattering cross section and internal electric energy using the finite-difference time-domain (FDTD) method for linearly polarized illumination at normal incidence in the 600- to 1000-nm wavelength range (more details about numerical simulations can be found in Materials and Methods). The linear refractive index data of MOCVD GaP used for the calculations were determined through spectral ellipsometry measurements (see note S1 for refractive index data). The obtained refractive index values were found to coincide with those from a commercial crystalline GaP wafer, within 2% (*32*). It is worth mentioning that other common fabrication techniques for growing GaP on a substrate, such as radio frequency magnetron sputtering (*34*), can only produce the material in an amorphous phase, which does not exhibit negligible linear absorption or as high refractive index values as the case of the MOCVD crystalline GaP used in this work. Figure 1B shows the simulated scattering cross section for the three disk diameters highlighted in Fig. 1A (D = 560, 600, and 640 nm), while Fig. 1C presents the computed electric energy and corresponding electric field distribution patterns for the case of D = 600 nm (refer to note S2 for electric energy calculations for other disk diameters). It can be seen that there are multiple optical modes confining the field inside the disk, implying that volumetric nonlinear effects can be greatly enhanced over the wavelength region of interest.

To characterize the nonlinear dynamics of the fabricated nanoantennas, we performed nondegenerate pump-probe spectroscopy measurements of individual nanodisks using sub–10-fs pulses (refer to Materials and Methods for specific details on pump-probe measurements). The spectral components of the pump and probe pulses covered the 600- to 750-nm and 750- to 1000-nm wavelength ranges, respectively, as shown in Fig. 1B (bottom). Figure 2 shows the measured differential reflectivity ($\Delta R/R$) response from three single nanoantennas as a function of probe wavelength (λ) and pump-probe delay time (t), at a pump peak energy density (P) of 10 pJ/μm^2 and a 5:1 pump-probe fluence ratio. A fixed reflectivity background introduced by the glass substrate surrounding the nanodisk scattering cross-sectional area was subtracted from the R data (see more details in Materials and Methods). In the three cases in Fig. 2, a strong negative $\Delta R/R$ signal is observed around t = 0 fs, at wavelengths near minima in the scattering cross section and maxima in the electric energy (see Fig. 1, B and C, and note S2), which we assign to the anapole excitation (AE). The AE is an optical state formed with leading contributions from the electric dipole and toroidal dipole modes and is characterized by a scattering minimum and an electric energy maximum, with a distinctive electric field pattern matching that in Fig. 1C (*5*, *6*, *35*, *36*). In Fig. 2, depending on the disk size, the $\Delta R/R$ peak response varies between −14 and −20% and vanishes within a 100-fs time period. We attribute this nearly instantaneous effect to the nonlinear OKE and TPA, as will be discussed later in this section. At longer delay times, at wavelengths in the vicinity of the ultrafast signals, we find the presence of smaller and much slower $\Delta R/R$ contributions. The effect is most evident in Fig. 2 (B and C) and only slightly noticed in Fig. 2A, where its magnitude is just about a tenth of the maximum response. Given the long time scale of these signals, which do not relax within the studied time window of 1.2 ps, we assign their origin to the relaxation of free carriers (FCs) (*37*), generated through TPA. We highlight, however, that near the center wavelengths of the ultrafast responses, no

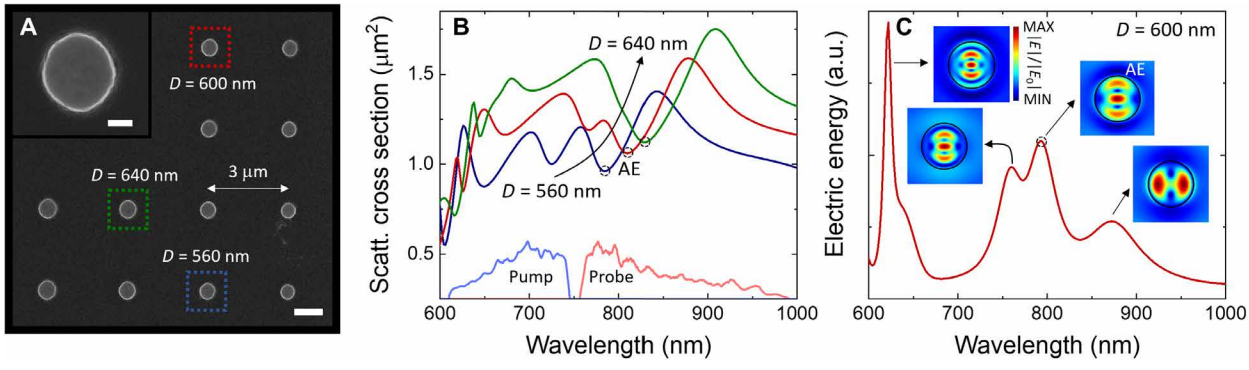

Fig. 1. Design and linear simulations of GaP nanoantennas. (**A**) Scanning electron microscopy image of the fabricated sample. The inset shows a magnified view of a nanodisk of 600-nm diameter. Scale bars, 1 μm (main image) and 200 nm (inset). (**B**) Simulated scattering (Scatt.) cross section for disks of 560-, 600-, and 640-nm diameter. AE denotes the anapole excitation (encircled minima). In the bottom of the graph, the pump and probe spectra are displayed in arbitrary intensity units. (**C**) Calculated electric energy for the D = 600-nm nanodisk, computed as $W_E \propto \iiint |E|^2 dV$, with V denoting the volume of the nanoantenna. The simulated electric field distributions corresponding to the most prominent peaks are included at selected disk heights presenting maximum field accumulation. From lowest to highest wavelength, corresponding height values as measured from the substrate are 25, 70, 20, and 5 nm. a.u., arbitrary units.

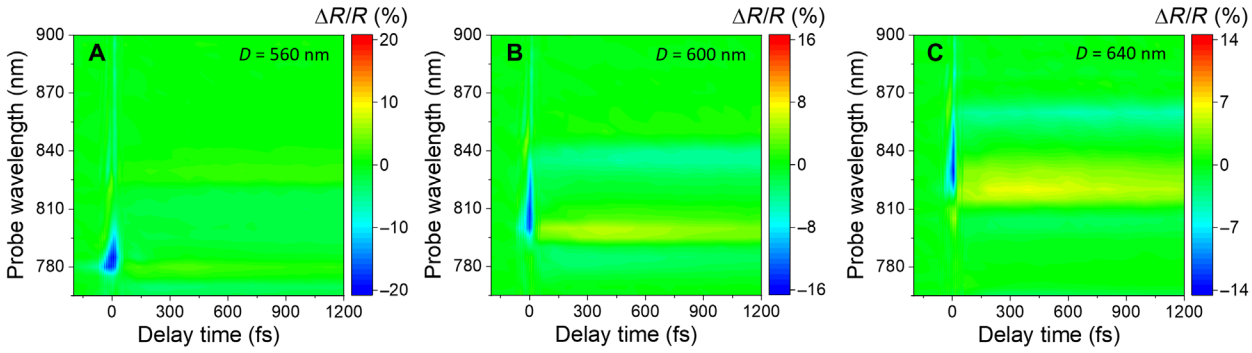

Fig. 2. Pump/probe spectroscopy results of single GaP nanodisks. (**A** to **C**) Differential reflectivity spectra of individual nanoantennas of diameters $D = 560$, 600, and 640 nm, registered by pumping the sample at $P = 10$ pJ/μm^2, with a 5:1 pump-probe fluence ratio.

FC effects are detected, making it possible to benefit from clean sub–100-fs modulations at specific wavelengths.

To model the ultrafast behavior of the dielectric nanoantennas, we performed nonlinear simulations including the OKE and TPA, considering average degenerate nonlinear values of $n_2 = 2 \times 10^{-18}$ m^2/W and β = 3 cm/GW as determined for crystalline GaP in this wavelength range (see Materials and Methods for details on nonlinear numerical simulations) (*32*). For the calculations, we approximated GaP complex refractive index as $\tilde{n} = (n_0 + ik_0) + I(n_2 + ik_2)$, where n_0 and k_0 denote the low-intensity real and imaginary components of the refractive index, respectively (with $k_0 = 0$ for GaP); I represents the intensity of the pump beam; and k_2 is the nonlinear absorption, which relates to β through the equation $k_2 = (\lambda\beta)/(4\pi)$. In this way, the OKE and TPA enabled modifications of GaP reflectivity through changes in the real and imaginary parts of $\tilde{n}$, respectively. Figure 3 compares the experimental and simulated differential reflectivity signals at $t = 0$ fs for the three studied nanodisks. Differences in the precise shape of the curves can be ascribed to simulations using constant average values of degenerate n_2 and β instead of the non-degenerate nonlinear parameters actually involved in the measurement, which may vary depending on the pair of pump and probe wavelengths. A good agreement is nevertheless obtained, with calculations correctly describing peak wavelength, modulation sign, and approximate magnitude of the measured responses. To determine the individual contributions of the different nonlinear effects to the total response, we performed a decomposition of the OKE and TPA on $\Delta R/R$, whose results are shown in the inset of Fig. 3B for the case of $D = 600$ nm. The simulation reveals that the OKE component, which increases the real part of $\tilde{n}$ ($n_2 > 0$), makes the anapole resonance more pronounced, decreasing R at AE wavelengths and increasing it at shorter and longer adjacent wavelengths. The TPA component, on the other hand, leads to a finite positive imaginary part of $\tilde{n}$ ($k_2 > 0$, $k_0 = 0$), lowering R at all wavelengths. Consequently, the combined response peaks at AE wavelengths, where both the OKE and TPA contribute with the same modulation sign. Their relative contribution is estimated to be approximately 40%/60% (OKE/TPA). It is worth mentioning here that the scattering and internal electric energy maxima at ~875 nm for $D = 600$ nm (Fig. 1, B and C) are found to produce no substantial effect in their corresponding $\Delta R/R$ response in Fig. 3. The nonlinear decomposition in the inset of Fig. 3B reveals that such maxima give rise to positive and negative shoulders in the OKE- and TPA-only responses, respectively, leading to a nearly zero $\Delta R/R$ net signal. This demonstrates

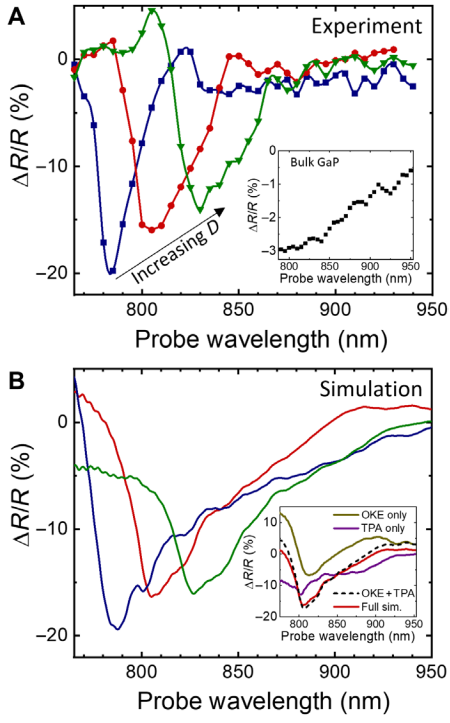

Fig. 3. Experimental and simulated nonlinear responses. (**A**) Experimental and (**B**) simulated differential reflectivity response at $t = 0$ fs and $P = 10$ pJ/μm^2 for $D = 560$ nm (blue), 600 nm (red), and 640 nm (green). The inset of (A) shows the registered response from a commercial double-sided polished 350-μm-thick GaP (100) wafer measured under the same experimental conditions. The inset of (B) exhibits the simulated response of the $D = 600$-nm antenna when considering the OKE contribution only ($n_2 = 2 \times 10^{-18}$ m^2/W and β = 0 cm/GW), the TPA contribution only ($n_2 = 0$ m^2/W and β = 3 cm/GW), their direct sum, and the full simulation (sim.) ($n_2 = 2 \times 10^{-18}$ m^2/W and β = 3 cm/GW). The latter matches the red curve in the main graph.

that a scattering maximum is not nearly as efficient as a scattering minimum for producing OKE/TPA nonlinear reflectivity modulations. For reference, the inset of Fig. 3A exhibits the measured $\Delta R/R$ signal at $t = 0$ fs for bulk GaP, displaying a maximum modulation of 3%, in absolute value, which monotonically decreases with increasing probe wavelength. This effect is thought to be a consequence of GaP linear refractive index decreasing with increasing wavelength, combined with nondegenerate n_2 and β diminishing for longer probe wavelengths. We note that this GaP intrinsic behavior is also present

in the response from the nanoantennas, as nanodisks featuring resonances at longer wavelengths are found to present a weaker signal. An additional factor contributing to the smallest nanodisk presenting the strongest modulation response is its relatively narrow resonance bandwidth, which makes it most sensitive to pump-induced $\tilde{n}$ changes.

To study the dependence of the magnitude of the ultrafast modulation signal on the pump peak energy density, we performed measurements of the three studied disks in the P range (0 to 20 pJ/μm^2) at specific probe wavelengths exhibiting no FC effects (λ = 785 nm for D = 560 nm, λ = 815 nm for D = 600 nm, and λ = 845 nm for D = 640 nm, as extracted from Fig. 2). The results are shown in Fig. 4A, where an approximately linear behavior of $|\Delta R/R|$ with P is found up to P = 10 pJ/μm^2 for all diameters. For P > 10 pJ/μm^2, the signals start to saturate, reaching maximum $|\Delta R/R|$ values of 37, 26, and 15% at 20 pJ/μm^2 for D = 560, 600, and 640 nm, respectively. In Fig. 4B, we evaluate the effect of the pump power on the time response of the modulation signals for selected cases. To determine characteristic times and modulation bandwidths, we performed fits to the data by convoluting exponential functions with the instrument response function, described by a Gaussian profile of 11-fs FWHM (*32*). Black and red curves in Fig. 4B show results for D = 600 nm at P = 10 and 20 pJ/μm^2, respectively. At P = 10 pJ/μm^2, we register a temporal FWHM (τ_{FWHM}) of 19 fs and a $1/e^2$ modulation bandwidth (ν_{MB}) of 18 THz (see note S3 for pump-probe temporal traces of other disk diameters at P = 10 pJ/μm^2). Corresponding values in the saturating range (P = 20 pJ/μm^2) are τ_{FWHM} = 26 fs and ν_{MB} = 12 THz. For D = 560 nm (blue curve in Fig. 4B), we find an even longer τ_{FWHM} = 66 fs (ν_{MB} = 5 THz), which can be understood from the smaller spectral bandwidth of this resonance compared to those of the other disks (see Figs. 2 and 3A). It should be noted that this performance represents a two orders of magnitude improvement with respect to previous reports on dielectric metasurfaces and nanoantennas for sub–100-fs all-optical switching (*2*, *3*). A direct-gap GaAs semiconductor metasurface demonstrated similar $\Delta R/R$ values, around 40%, but with the consequence of much longer characteristic modulation times of several picoseconds due to FC effects (*37*). It should also be mentioned that the fastest reported plasmonic-based nanoscale approaches featuring 20% modulation depth or more (*38*, *39*) showed τ_{FWHM} values about one order of magnitude larger compared to the GaP nanodisk (refer to note S4 for a more detailed comparison).

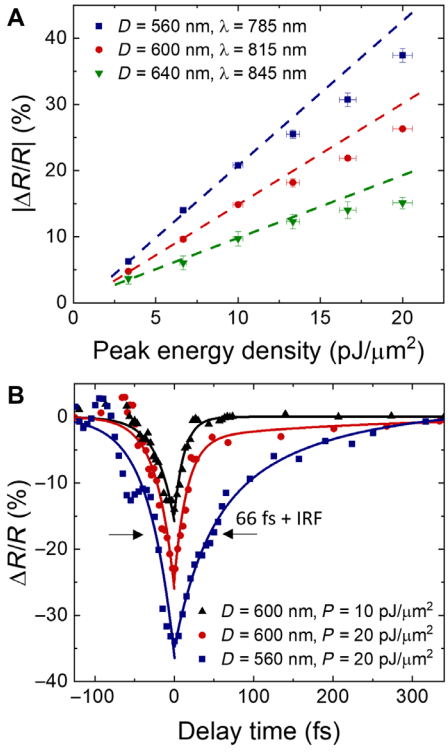

Fig. 4. Modulation performance at different pump powers. (**A**) Pump peak energy density dependence of $|\Delta R/R|$ at selected probe wavelengths for nanoantennas with D = 560 nm (λ = 785 nm), D = 600 nm (λ = 815 nm), and D = 640 nm (λ = 845 nm). (**B**) Corresponding temporal trace results at specific pump peak energy densities detailed in the graph for the two most efficient disks. Solid lines correspond to exponential fits to the experimental data. IRF, instrument response function.

In summary, we have demonstrated that resonant single GaP nanodisks with negligible linear absorption can produce $1/e^2$ modulation bandwidths of 5, 12, and 18 THz, with approximate maximum modulation depths of 40, 25, and 15%, respectively, depending on pump power, disk size, and probe wavelength. The observed sub–100-fs effect is modeled through nonlinear-induced variations of GaP complex refractive index due to the OKE and TPA, with a relative contribution of around 40%/60% (OKE/TPA). We find that the ultrafast response occurs in the vicinity of the AE scattering minimum, at wavelengths where TPA-induced FC effects are found to be negligible. We also find that modes featuring scattering maxima do not produce substantial differential reflectivity modulations, as they give rise to OKE and TPA signals with opposite responses. The findings from this investigation open new possibilities for the optimization of nonlinear all-optical modulators and place the GaP nanodisk as the most efficient nanoscale all-optical switch at sub–100-fs time scales demonstrated to date, to the best of our knowledge.

MATERIALS AND METHODS

Nanofabrication

GaP nanodisks were fabricated on a SiO_2-on-sapphire substrate, starting from a commercially available MOCVD-grown crystalline GaP layer (~400 nm) on a GaAs substrate. The latter structure was directly bonded to the sapphire substrate after depositing ~5-μm SiO_2 layers on top of both surfaces. The GaAs substrate was later removed by wet etching. The fabrication of the GaP nanodisks started with a standard wafer cleaning procedure (acetone, isopropyl alcohol, and deionized water in that sequence under sonication). The GaP layer was then thinned down to a thickness of 200 nm by inductively coupled plasma reactive ion etching (ICP-RIE) with N_2 and Cl_2 gases. The following step involved O_2 and hexamethyl disilizane (HMDS) priming to increase the adhesion between GaP and the subsequently spin-coated EBL resist of hydrogen silsesquioxane (HSQ). After spin-coating of the HSQ layer with a thickness of ~150 nm, EBL and development in 25% tetramethyl ammonium hydroxide (TMAH) were carried out to define the nanodisks in the HSQ resist. Last, ICP-RIE with N_2 and Cl_2 gases was used again to transfer the HSQ patterns to the GaP layer and generate the GaP nanodisk structures.

Pump-probe experiments

A pulsed Yb:KGW Pharos laser system coupled to a collinear optical parametric amplifier ORPHEUS-HP (Light Conversion Ltd.; pulse

duration of ~180 fs, repetition rate of 200 kHz) was used to generate supercontinuum light by focusing a 1120-nm wavelength beam at 600-mW average power onto a 5-mm-thick sapphire plate. The supercontinuum beam was split into ~600- to 750-nm and ~750- to 1000-nm spectral components using dichroic beam splitters (see spectra of pump and probe pulses in Fig. 1B). The wide-spectrum beams were coupled to a MIIPS (multiphoton intrapulse interference phase scan) device (MIIPSBox640-P by Biophotonic Solutions Inc.), able to compress the pulses in time down to bandwidth-limited ~7-fs pulses at the position of the sample. A motorized optical delay line was used to introduce controlled time differences between the different trains of pulses with <1-fs accuracy. The two pulsed beams were focused onto the sample using a metal objective of 0.5 numerical aperture. The measurements were carried out with lock-in detection by modulating the pump beam at <1-kHz frequency using an optical chopper. A spectrograph (PI Acton SP2300 by Princeton Instruments) coupled to a low-noise Si photodiode (picowatt photoreceiver series PWPR-2K by Femto) was used for spectral characterization of the probe light reflected by the sample.

The constant reflectivity background (R_B) produced by the glass substrate around the nanoantenna's scattering cross-sectional region was subtracted from the measured R values. R_B was calculated as the product R_G*P_G, where R_G denotes glass reflectivity and P_G represents the proportion of probe power illuminating the substrate surrounding the nanodisk scattering cross-sectional area.

More details on the creation of ultrashort pulses and the pump-probe method can be found published elsewhere (*3*, *32*).

Numerical simulations

The nonlinear numerical simulations were performed with the FDTD technique using the commercial software Lumerical FDTD Solutions, with an instantaneous OKE and TPA implemented following the formalism of Suzuki (*40*) [more details on the simulations and the nonlinear implementation can be found elsewhere (*32*)]. The linearly polarized pulses were inputted via Gaussian focusing using a numerical aperture of 0.5 and with the focal position located at the mid-height of the nanodisks, in agreement with the experimental conditions. Perfectly matched layers were used as the simulation boundary conditions to avoid reflections. The experimental spectra for the pump-probe pulses (as seen in Fig. 1B) were imported into the FDTD simulations as custom sources, which resulted in ripples in the simulated differential reflectivity curves, which were removed by smoothing through adjacent averaging. It should be noted that replacing the custom sources by standard Gaussian spectra sources with the same temporal duration resulted in smoother differential reflectivity curves but gave poor agreement with the experimental results. Ellipsometry measurements were used to determine the linear optical properties of MOCVD GaP (see note S1), with the software built-in optical properties used for the SiO_2 substrate. The nonlinear parameters of GaP of $n_2 = 2 \times 10^{-18}$ m^2/W and $\beta = 3$ cm/GW were used in agreement with the results from our previous work (*32*), with the input pump and probe powers matched to the experimental conditions. No nonlinear effects were assumed for the underlying SiO_2 substrate. For the linear simulations depicted in Fig. 1, the nanodisks were illuminated by broadband linearly polarized plane waves at normal incidence. The electric energy inside the GaP nanodisk was calculated using monitors placed around the nanodisk to define the volume V.

SUPPLEMENTARY MATERIALS

Supplementary material for this article is available at http://advances.sciencemag.org/cgi/content/full/6/34/eabb3123/DC1

REFERENCES AND NOTES

1. R. W. Boyd, *Nonlinear Optics* (Academic Press, ed. 3, 2008).
2. M. R. Shcherbakov, P. P. Vabishchevich, A. S. Shorokhov, K. E. Chong, D. Y. Choi, I. Staude, A. E. Miroshnichenko, D. N. Neshev, A. A. Fedyanin, Y. S. Kivshar, Ultrafast all-optical switching with magnetic resonances in nonlinear dielectric nanostructures. *Nano Lett.* **15**, 6985–6990 (2015).
3. G. Grinblat, R. Berte, M. P. Nielsen, Y. Li, R. F. Oulton, S. A. Maier, Sub-20 fs all-optical switching in a single au-clad si nanodisk. *Nano Lett.* **18**, 7896–7900 (2018).
4. J. Cambiasso, G. Grinblat, Y. Li, A. Rakovich, E. Cortes, S. A. Maier, Bridging the gap between dielectric nanophotonics and the visible regime with effectively lossless gallium phosphide antennas. *Nano Lett.* **17**, 1219–1225 (2017).
5. G. Grinblat, Y. Li, M. P. Nielsen, R. F. Oulton, S. A. Maier, Efficient third harmonic generation and nonlinear subwavelength imaging at a higher-order anapole mode in a single germanium nanodisk. *ACS Nano* **11**, 953–960 (2017).
6. G. Grinblat, Y. Li, M. P. Nielsen, R. F. Oulton, S. A. Maier, Enhanced third harmonic generation in single germanium nanodisks excited at the anapole mode. *Nano Lett.* **16**, 4635–4640 (2016).
7. L. Xu, M. Rahmani, K. Zangeneh Kamali, A. Lamprianidis, L. Ghirardini, J. Sautter, R. Camacho-Morales, H. Chen, M. Parry, I. Staude, G. Zhang, D. Neshev, A. E. Miroshnichenko, Boosting third-harmonic generation by a mirror-enhanced anapole resonator. *Light Sci. Appl.* **7**, 44 (2018).
8. R. Camacho-Morales, M. Rahmani, S. Kruk, L. Wang, L. Xu, D. A. Smirnova, A. S. Solntsev, A. Miroshnichenko, H. H. Tan, F. Karouta, S. Naureen, K. Vora, L. Carletti, C. De Angelis, C. Jagadish, Y. S. Kivshar, D. N. Neshev, Nonlinear generation of vector beams from algaas nanoantennas. *Nano Lett.* **16**, 7191–7197 (2016).
9. G. Grinblat, Y. Li, M. P. Nielsen, R. F. Oulton, S. A. Maier, Degenerate four-wave mixing in a multiresonant germanium nanodisk. *ACS Photonics* **4**, 2144–2149 (2017).
10. Y. Yang, W. Wang, A. Boulesbaa, I. I. Kravchenko, D. P. Briggs, A. Puretzky, D. Geohegan, J. Valentine, Nonlinear fano-resonant dielectric metasurfaces. *Nano Lett.* **15**, 7388–7393 (2015).
11. K. H. Kim, W. S. Rim, Strongly resonant metasurfaces supported by reflective substrates for highly efficient second- and high-harmonic generations with ultralow pump intensity. *Phys. Chem. Chem. Phys.* **21**, 19076–19082 (2019).
12. G. Marino, C. Gigli, D. Rocco, A. Lemaître, I. Favero, C. De Angelis, G. Leo, Zero-order second harmonic generation from algaas-on-insulator metasurfaces. *ACS Photonics* **6**, 1226–1231 (2019).
13. M. Semmlinger, M. Zhang, M. L. Tseng, T. T. Huang, J. Yang, D. P. Tsai, P. Nordlander, N. J. Halas, Generating third harmonic vacuum ultraviolet light with a tio2 metasurface. *Nano Lett.* **19**, 8972–8978 (2019).
14. M. Timofeeva, L. Lang, F. Timpu, C. Renaut, A. Bouravleuv, I. Shtrom, G. Cirlin, R. Grange, Anapoles in free-standing iii–v nanodisks enhancing second-harmonic generation. *Nano Lett.* **18**, 3695–3702 (2018).
15. P. P. Vabishchevich, S. Liu, M. B. Sinclair, G. A. Keeler, G. M. Peake, I. Brener, Enhanced second-harmonic generation using broken symmetry iii–v semiconductor fano metasurfaces. *ACS Photonics* **5**, 1685–1690 (2018).
16. R. Colom, L. Xu, L. Marini, F. Bedu, I. Ozerov, T. Begou, J. Lumeau, A. E. Miroshnishenko, D. Neshev, B. T. Kuhlmey, S. Palomba, N. Bonod, Enhanced four-wave mixing in doubly resonant si nanoresonators. *ACS Photonics* **6**, 1295–1301 (2019).
17. T. Shibanuma, G. Grinblat, P. Albella, S. A. Maier, Efficient third harmonic generation from metal-dielectric hybrid nanoantennas. *Nano Lett.* **17**, 2647–2651 (2017).
18. S. Liu, P. P. Vabishchevich, A. Vaskin, J. L. Reno, G. A. Keeler, M. B. Sinclair, I. Staude, I. Brener, An all-dielectric metasurface as a broadband optical frequency mixer. *Nat. Commun.* **9**, 2507 (2018).
19. M. R. Shcherbakov, K. Werner, Z. Fan, N. Talisa, E. Chowdhury, G. Shvets, Photon acceleration and tunable broadband harmonics generation in nonlinear time-dependent metasurfaces. *Nat. Commun.* **10**, 1345 (2019).
20. H. Liu, C. Guo, G. Vampa, J. L. Zhang, T. Sarmiento, M. Xiao, P. H. Bucksbaum, J. Vučković, S. Fan, D. A. Reis, Enhanced high-harmonic generation from an all-dielectric metasurface. *Nat. Phys.* **14**, 1006–1010 (2018).
21. G. Li, S. Zhang, T. Zentgraf, Nonlinear photonic metasurfaces. *Nat. Rev. Mater.* **2**, 17010 (2017).
22. A. I. Kuznetsov, A. E. Miroshnichenko, M. L. Brongersma, Y. S. Kivshar, B. Luk'yanchuk, Optically resonant dielectric nanostructures. *Science* **354**, aag2472 (2016).
23. M. R. Shcherbakov, D. N. Neshev, B. Hopkins, A. S. Shorokhov, I. Staude, E. V. Melik-Gaykazyan, M. Decker, A. A. Ezhov, A. E. Miroshnichenko, I. Brener, A. A. Fedyanin, Y. S. Kivshar, Enhanced third-harmonic generation in silicon nanoparticles driven by magnetic response. *Nano Lett.* **14**, 6488–6492 (2014).

24. R. Camacho-Morales, G. Bautista, X. Zang, L. Xu, L. Turquet, A. Miroshnichenko, H. H. Tan, A. Lamprianidis, M. Rahmani, C. Jagadish, D. N. Neshev, M. Kauranen, Resonant harmonic generation in algaas nanoantennas probed by cylindrical vector beams. *Nanoscale* **11**, 1745–1753 (2019).
25. V. Remesh, G. Grinblat, Y. Li, S. A. Maier, N. F. van Hulst, Coherent multiphoton control of gallium phosphide nanodisk resonances. *ACS Photonics* **6**, 2487–2491 (2019).
26. S. D. Gennaro, M. Rahmani, V. Giannini, H. Aouani, T. P. Sidiropoulos, M. Navarro-Cia, S. A. Maier, R. F. Oulton, The interplay of symmetry and scattering phase in second harmonic generation from gold nanoantennas. *Nano Lett.* **16**, 5278–5285 (2016).
27. H. Aouani, M. Navarro-Cia, M. Rahmani, T. P. Sidiropoulos, M. Hong, R. F. Oulton, S. A. Maier, Multiresonant broadband optical antennas as efficient tunable nanosources of second harmonic light. *Nano Lett.* **12**, 4997–5002 (2012).
28. M. Lippitz, M. A. van Dijk, M. Orrit, Third-harmonic generation from single gold nanoparticles. *Nano Lett.* **5**, 799–802 (2005).
29. Z. Chai, X. Hu, F. Wang, X. Niu, J. Xie, Q. Gong, Ultrafast all-optical switching. *Adv. Opt. Mater.* **5**, 1600665 (2017).
30. G. T. Reed, G. Mashanovich, F. Y. Gardes, D. J. Thomson, Silicon optical modulators. *Nat. Photonics* **4**, 518–526 (2010).
31. L. Zhang, M. Agarwal Anuradha, C. Kimerling Lionel, J. Michel, Nonlinear group iv photonics based on silicon and germanium: From near-infrared to mid-infrared. *Nanophotonics* **3**, 247–268 (2014).
32. G. Grinblat, M. P. Nielsen, P. Dichtl, Y. Li, R. F. Oulton, S. A. Maier, Ultrafast sub-30 fs all- optical switching based on gallium phosphide. *Sci. Adv.* **5**, eaaw3262 (2019).
33. D. J. Wilson, K. Schneider, S. Hönl, M. Anderson, Y. Baumgartner, L. Czornomaz, T. J. Kippenberg, P. Seidler, Integrated gallium phosphide nonlinear photonics. *Nat. Photonics* **14**, 57–62 (2020).
34. J. Gao, Q. Zhan, A. M. Sarangan, High-index low-loss gallium phosphide thin films fabricated by radio frequency magnetron sputtering. *Thin Solid Films* **519**, 5424–5428 (2011).
35. A. E. Miroshnichenko, A. B. Evlyukhin, Y. F. Yu, R. M. Bakker, A. Chipouline, A. I. Kuznetsov, B. Luk'yanchuk, B. N. Chichkov, Y. S. Kivshar, Nonradiating anapole modes in dielectric nanoparticles. *Nat. Commun.* **6**, 8069 (2015).
36. F. Monticone, D. Sounas, A. Krasnok, A. Alù, Can a nonradiating mode be externally excited? Nonscattering states versus embedded eigenstates. *ACS Photonics* **6**, 3108–3114 (2019).
37. M. R. Shcherbakov, S. Liu, V. V. Zubyuk, A. Vaskin, P. P. Vabishchevich, G. Keeler, T. Pertsch, T. V. Dolgova, I. Staude, I. Brener, A. A. Fedyanin, Ultrafast all-optical tuning of direct-gap semiconductor metasurfaces. *Nat. Commun.* **8**, 17 (2017).
38. P. Guo, R. D. Schaller, J. B. Ketterson, R. P. H. Chang, Ultrafast switching of tunable infrared plasmons in indium tin oxide nanorod arrays with large absolute amplitude. *Nat. Photonics* **10**, 267–273 (2016).
39. M. Z. Alam, S. A. Schulz, J. Upham, I. De Leon, R. W. Boyd, Large optical nonlinearity of nanoantennas coupled to an epsilon-near-zero material. *Nat. Photonics* **12**, 79–83 (2018).
40. N. Suzuki, Fdtd analysis of two-photon absorption and free-carrier absorption in si high-index-contrast waveguides. *J. Lightwave Technol.* **25**, 2495–2501 (2007).

Acknowledgments

Funding: This work was supported by the Quantum Technology for Engineering (QTE) program of the A*STAR (Singapore) and the A*STAR SERC Pharos program, grant no. 152 73 00025 (Singapore). G.G. and E.C. acknowledge support from the PICT grant no. 2017-2534. S.A.M., Y.L., and E.C. acknowledge the Deutsche Forschungsgemeinschaft (German's Excellence Strategy EXC 2089/1–390776260). S.A.M. further acknowledges the EPSRC (EP/M013812/1) and the Lee-Lucas Chair in Physics. Y.L. also acknowledges funding received from the European Union's Framework Programme for Research and Innovation Horizon 2020 (2014–2020) under the Marie Skłodowska-Curie grant agreement no. 754388 (LMU Research Fellowships). M.P.N. would like to thank the UNSW Scientia Fellowship Program for ongoing support. **Author contributions:** G.G. conceived the idea and A.I.K. proposed the collaboration. Y.L. calculated the optical resonances and laid out the design of the nanoantenna arrays. H.Z., L.K., and A.I.K. developed the nanofabrication process, which A.I.K. supervised. H.Z. performed the nanofabrication of the samples. G.G., R.B., and B.T. performed the pump-probe experiments. M.P.N. performed the numerical simulations with input from Y.L. G.G. analyzed the data and wrote the manuscript with input from all authors. **Competing interests:** The authors declare that they have no competing interests. **Data and materials availability:** All data needed to evaluate the conclusions in the paper are present in the paper and/or the Supplementary Materials. Additional data that support the findings of this study are available from the corresponding author upon reasonable request.

Submitted 14 February 2020
Accepted 9 July 2020
Published 21 August 2020
10.1126/sciadv.abb3123

Citation: G. Grinblat, H. Zhang, M. P. Nielsen, L. Krivitsky, R. Berté, Y. Li, B. Tilmann, E. Cortés, R. F. Oulton, A. I. Kuznetsov, S. A. Maier, Efficient ultrafast all-optical modulation in a nonlinear crystalline gallium phosphide nanodisk at the anapole excitation. *Sci. Adv.* **6**, eabb3123 (2020).